# Effects of the pretreatment of CuNi/SiO2 on ethanol steam reforming: Influence of bimetal morphology

Li-Chung Chen, Shawn D. Lin*

Department of Chemical Engineering, National Taiwan University of Science and Technology, Taipei 106, Taiwan, ROC

ABSTRACT

Previous research shows that bimetallic CuNi/SiO2 catalysts prepared by NaBH4 reduction perform well in ethanol steam reforming (ESR) compared to their monometallic counterparts. More importantly, these bimetallic catalysts yield simple products of only $H_2$, $CO_2$, $CO$, and $CH_4$, at high ethanol conversions. The as-prepared catalysts contain mainly alloy nanoparticles. This study shows that ESR performance can be further improved by catalyst pretreatment, i.e., calcination at 400 °C followed by reduction at 350 °C (coded hereafter as calc-CuNi-R350). Characterization using in situ X-ray diffraction (XRD) and X-ray absorption fine structure (XAFS) indicates that the calc-CuNi-R350 catalyst contains Cu-rich nanoparticles in close proximity to NiO nanocrystals. Compared to the uncalcined but reduced catalyst (asis-CuNi-R350), the calc-CuNi-R350 catalyst had higher turnover frequency for ethanol conversion and for acetaldehyde conversion and lower selectivity to $CH_4$ formation. Increasing the steam/ethanol (S/E) ratio from 6 to 9 significantly suppresses $CH_4$ formation from this calc-CuNi-R350 catalyst. The results of this study suggest that the interface between NiO and Cu-rich nanoparticles improves ASR/AD (acetaldehyde steam reforming/acetaldehyde decomposition) selectivity via stabilizing the methyl (or methylene) groups from the decomposition of acetaldehyde intermediate and consequently decreases the probability of $CH_4$ evolution. If $CH_4$ evolution is suppressed, the ESR reaction produces only $H_2$, $CO$, and $CO_2$. This makes ESR an attractive sustainable route for $H_2$ production.

© 2013 Elsevier B.V. All rights reserved.

## 1. Introduction

Currently, methane steam reforming is largely used for commercial hydrogen production and methanol steam reforming (MSR) is extensively studied for boosting devices such as fuel cells. Bioethanol is considered a carbon-neutral fuel and therefore ethanol steam reforming (ESR) is a sustainable method for producing hydrogen. ESR derives many side products other than the expected $H_2$ and $CO_2$ and its reaction pathways and mechanism have recently been reviewed [1]. The more complicated reaction pathway of ESR compared to MSR arises from the necessity to break the C—C bond of ethanol. The much-used Cu catalysts for MSR are ineffective to break the C—C bond while Ni, Co, Ir, and Rh are effective [2,3]. Ni is relatively inexpensive and therefore many tests of Ni catalysts for ESR have been reported. However, coke formation is severe in ESR over Ni catalysts. Two approaches are typically adopted to resolve this problem, namely, using bimetal (or multi-metal) catalysts and using active support such as $CeO_2$ which can contribute lattice oxygen to enhance steam reforming. Trimm [4,5] mentioned that $CeO_2$ support can decrease the

coke formation over Ni catalysts during steam reforming. Choi et al. [6] reported that $Ni/CeO_2$–$Al_2O_3$ had a lower coking tendency than $Ni/Al_2O_3$ during isooctane autothermal reforming. When a second metal is used, the type of metal, the composition and the alloy formation are key factors determining the catalytic performance [7]. Different metals have been reported to cope with Ni for ESR, such as Co, Cu, Rh, Pt. Among these second metals, Cu is relatively inexpensive and it enhances ESR performance with decreased coking tendency [8–14]. In general, ESR performance can be rated by the ethanol conversion rate, the hydrogen yield and the coking tendency of catalyst. We reported previously that a Cu/Ni ratio of 1 resulted in better ESR performance than other Cu/Ni composition over the CuNi/SiO2 catalyst prepared by NaBH4 reduction [11]. However, the optimal Cu/Ni composition seems to depend on the type of support, the catalyst preparation method and even the operating temperature. For example, Fierro et al. [15] reported that Cu doped $Ni/Al_2O_3$ showed the highest $H_2$ selectivity for oxidative ESR at 923 K but it became the worst comparing to that doped with Zn, Fe, and Cr when operated at 1073 K. Mariño et al. [8–10] examined the effect of adding Cu to $4\%Ni/K$–$Al_2O_3$ and reported that 2% Cu addition showed the highest hydrogen yield. Wang reported that $10\%Ni$–$5\%Cu/MgO$–$Al_2O_3$ was superior to catalysts with different Cu/Ni ratio [16]. De Rogatis et al. [14] reported that the ESR

* Corresponding author. Tel.: +886 2 27376984; fax: +886 2 27376644.
E-mail address: sdlin@mail.ntust.edu.tw (S.D. Lin).

product distribution was not significantly changed by the Cu/Ni ratio of $Al_2O_3$-supported CuNi catalysts. The formation of Cu–Ni alloy was considered beneficial for ESR [12,14,17]. However, the different Cu/Ni ratios reported in these references imply a need to resolve the active bimetallic structure such that the catalyst can be improved further.

The other approach utilizes the metal–support interaction to enhance the ESR performance and the stability of Ni catalysts. Support can have significant influence on the catalytic performance; for example, using acidic support can cause more dehydration and dehydrogenation during ESR which lead to high coking tendency. Additives such as K, Mg, and La are frequently used to modify $Al_2O_3$ support where an optimal amount of basic additives is frequently sought after. Youn et al. [18] reported that the best oxidative ESR performance can be obtained when using an intermediate acidity support for Ni catalysts, whereas Furtado et al. [19] reported that the acidity of support had no effect on the oxidative ESR over NiCu catalysts. Additives not only change acid–base property but can also influence Ni dispersion [20,21], create a carbon reservoir [22], or provide high-temperature stability [21,23]. The multiple roles that the additive may play make its optimization a complex issue. Another type of supports used for suppressing coke formation is reducible oxides, where surface oxygen from oxide may participate and consequently enhance reaction performance. Xu et al. examined $Ni/CeO_2$ for ESR and proposed that Ce(III) at $Ni$-$CeO_2$ interface can provide OH groups to react with the methyl groups from C—C bond breaking over Ni metal [24]. However, formation of $CH_4$ and coke are still present under their test conditions. Similar uses of reducible oxide support for mono- and bi-metallic catalysts have been reported for enhancing ESR reaction. For example, $Ce_xZr_{1-x}O_2$ has been examined as the support for Ni [25] and $CeO_2$ [26], $Ce_xZr_{1-x}O_2$ [27], and $CeGdO_x$ [28] for CuNi catalysts. In such cases of using reducible oxide support, increasing metal–support interface is usually the primary concern in catalyst preparation and the promoting effect is usually attributed qualitatively to the participation of surface oxygen.

Although different catalysts have been reported for ESR, ESR is not as efficient a hydrogen production reaction as MSR. ESR usually runs at a much higher steam ratio and a much higher reaction temperature than MSR. Though high reaction temperatures increase cracking activity, they also lead to coke formation and high energy consumption. The reverse water gas shift reaction is also favored at high temperatures, resulting in increased $CO/H_2$ ratio that may not be suitable for downstream uses such as fuel cells. Palma and co-workers [29–32] recently addressed the advantages of decreasing the reaction temperature of ESR and $Pt/CeO_2$ and $Pt$-$Ni/CeO_2$ were reported as effective catalysts. Approaches such as using membrane reactor to promote ESR were also reported [33,34] for decreasing the reaction temperature of ESR. Lower reaction temperatures are desirable and ideally, ESR products should include only $H_2$, CO, and $CO_2$, as in the case of MSR. If successful, this would make ESR an effective and sustainable route for $H_2$ production. Our previous report demonstrated that using Cu–Ni bimetallic catalysts can limit the ESR products to include only $H_2$, CO, $CO_2$, and $CH_4$ [11], and a reaction scheme (Scheme 1) was proposed. Reducing $CH_4$ formation is a prerequisite to simplifying Scheme 1 and improving ESR performance for $H_2$ production. This study reports that $CH_4$ formation can be reduced, though not eliminated, by changing the pretreatment of 5% $Cu_1Ni_1/SiO_2$ catalyst. Morphology characterization by TPR, XRD, and EXAFS suggests that mixed phases in $Cu_1Ni_1/SiO_2$ achieve more efficient ESR than the alloy phase. This is attributed to the enhanced acetaldehyde steam reforming and the enhanced water gas shift pathways of Scheme 1 by the presence of alloy–NiO interface.
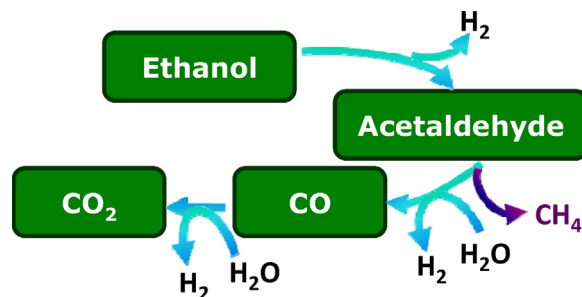


**Scheme 1.** A simple ESR reaction pathway.

## 2. Experimental

### 2.1. Preparation of catalysts

Supported 5 wt.% Cu, Ni, and bimetallic Cu–Ni (1/1) catalysts were prepared [11] by incipient-wetness impregnation of metal (Cu and Ni) nitrate (Aldrich, 98%) aqueous solution on $SiO_2$ support (Davison 952, 300 m$^2$/g, used after calcinations at 550 °C). After impregnation, catalysts were dried at 25 °C under rough vacuum generated by a rotary pump. Each catalyst was then dispersed in $H_2O$ and stirred for 10 min. A 5% $NaBH_4$ (diluted from Aldrich, 98.5%) solution was then added drop-by-drop at room temperature until $NaBH_4$/metal = 5 (molar ratio) [11]. After additional stirring for 30 min, the solid was recovered by centrifugation, washed thoroughly with $H_2O$ and then vacuum dried at room temperature. The supernatant was examined by ICP-AES and no loss of Cu or Ni was evident. The as-prepared catalysts (denoted as asis-) were then calcined in air at 400 °C for 5 h (denoted as calc-).

### 2.2. Characterizations

Temperature-programmed reduction (TPR) analysis was performed at 5 °C/min using 10% $H_2$ in nitrogen and a TCD detector; the $H_2O$ formed during TPR was trapped by a molecular sieve column installed prior to the detector. The catalyst was typically purged by He at 50 °C till TCD became stable and then switched to $H_2/N_2$ flow and the temperature was ramped. For metal surface area analysis, the catalyst was pretreated by $H_2$ flow at the target temperature for 1 h, cooled to 25 °C under He, and then subjected to $N_2O$ flow (50 mL/min) at 25 °C for 30 min. The catalyst bed was then purged with He and the $O_{ad}$ from $N_2O$ adsorption was quantitatively analyzed by the $H_2$ consumption in a subsequent TPR experiment. Metal dispersion was calculated by assuming an $O_{ad}/M_S$ ratio of 1/2, where $M_S$ represents the surface atoms of either Cu or Ni. This $O_{ad}/M_S$ stoichiometry of 1/2 is typically used for the evaluation of $Cu_S$ but it was doubted for $Ni_S$ due to the possible exchange of surface and subsurface oxygen over Ni [35]. However, the metal dispersion obtained by assuming $O_{ad}/M_S = 1/2$ is close to the calculated dispersion of Cu (or Ni) particles based on the average size obtained from XRD and TEM [11].

In situ XRD was performed using the beamline BL01C at the National Synchrotron Radiation Research Center (NSRRC) in Hsinchu, Taiwan. The electron storage ring operated at 1.5 GeV with a beam current of 200 mA. The XRD pattern was recorded using a wavelength of 0.5167 Å for limited angular regions at room temperature. The recorded diffraction was corrected to that of Cu K$\alpha$1 radiation at a wavelength of 1.5418 Å. Diffraction patterns were obtained at a scan rate of 10°/min with steps of 0.05° in the 2$\theta$ range from 20° to 90°. EXAFS experiments were also performed using the BL17C beamline at the NSRRC. The Ni K-edge and Cu K-edge absorbance were measured sequentially in transmission mode at room temperature. In situ analysis was carried out in a stainless

steel cell with a Krypton film cap on two windows to allow a transmission beam path under controlled atmosphere. EXAFS data were analyzed using Artemis analysis programs with $k^2$-weighting of data in k-space ranging from 3 to 10.5 Å$^{-1}$ and from 3.0 to 13.5 Å$^{-1}$ for the Ni K-edge and the Cu K-edge, respectively. A nonlinear least-squares curve fitting was performed in r-space ranging from 1.0 to 3.0 Å for Cu and from 1.0 to 3.8 Å for Ni.

### 2.3. Catalytic ESR test

Reaction tests were performed in a quartz-tube packed-bed reactor at atmospheric pressure. In each experiment, 0.1 g of the catalyst was sandwiched between quartz wool, installed in a home-made system, and reduced with 20 vol% $H_2/N_2$ (50 ml/min) at selected temperature for 1 h. The ethanol aqueous solution with $H_2O$/ethanol = 6 or 9 was fed by a syringe pump and carried by a He flow into the reactor at a EtOH partial pressure of 5.67 kPa (42.5 Torr) and a WHSV (weight hourly space velocity, g EtOH/g catalyst h) of 2 h$^{-1}$. Both He and $H_2$ were of 99.995% purity and were flown through dryer and Oxytrap columns before entering the system. The reaction was carried out in a temperature-programmed mode at 1 °C/min from 150 to 500 °C. The reactor effluent was analyzed using gas chromatography (Acme 6100) with a pulsed discharge helium ionization detector (PDHID) and two columns of a molecular-sieve one and a Porapak-N one. A 10-port switching valve is used for sampling and for switching the column sequence. The mass balance of the effluent was typically within ±10% of the feed for most catalysts at temperatures below 400 °C. For kinetic studies, steady state activity was recorded with $H_2O$/EtOH = 6 or $H_2O$/acetaldehyde = 6 at isothermal conditions and at conversions below 15% which was achieved by tuning space velocity. Steady state performance was observed typically from 30 to 90 min on stream and the average performance during that period is used for kinetic data analysis. Turnover frequency was calculated by using the metal surface measured by $N_2O$ adsorption assuming $O_{ad}/M_s = 1/2$.

## 3. Results

### 3.1. TPR analysis

Previous research [11] indicates that 5% $Cu_xNi_y/SiO_2$ with a composition of Cu/Ni = 1/1 leads to the highest ethanol steam reforming activity. The present study uses the same catalyst to examine the influence of calcination pretreatment. The reduction of the 5% $CuNi/SiO_2$ catalysts before and after calcination at 400 °C was investigated by TPR, and Fig. 1 shows their results in comparison to monometallic catalysts prepared using the same procedure. The asis-Cu catalyst had a main reduction peak at approximately 228 °C due to oxidized surface produced from air exposure [11]. The asis-Ni catalyst showed two broad reduction peaks at 280–450 and 450–630 °C respectively, attributable to the reduction of dispersed $NiO_x$ (or oxidized surface) and oxidized Ni with Ni-SiO$_2$ interaction [36], respectively. Both asis-CuNi and calc-CuNi catalysts had similar reduction peaks attributable to oxidized surface at below 200 °C, and to the oxidized Ni with Ni–SiO$_2$ interaction at around 570 °C. That the surface oxide reduction of asis-CuNi shifted to lower temperatures (at 158 °C) may be attributed to a high dispersion. Table 1 shows that the calc-CuNi catalyst consumed more $H_2$ from 50 to 250 °C than all other samples, as expected for its calcination pretreatment. The asis-CuNi had the lowest $H_2$ consumption in the same range suggesting a less-oxidized surface after air exposure which may be due to Ni addition. The two CuNi catalysts were reduced at 350 and 650 °C respectively and then tested for ESR. The former reduction temperature is the same as that used in our previous work [11] while TPR shows that the latter reduction temperature can result in complete reduction.
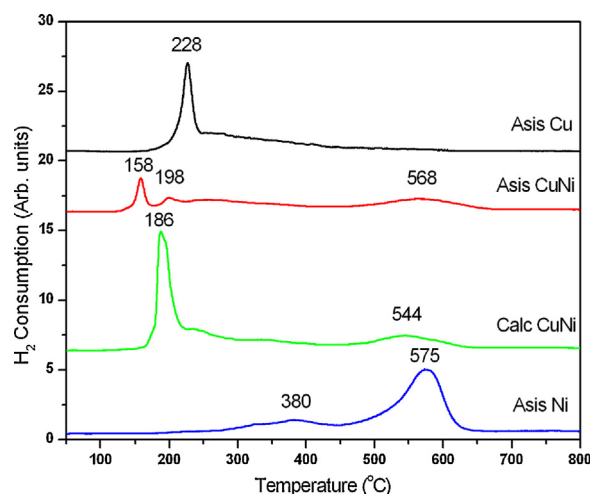


**Fig. 1.** Temperature programmed reduction profiles for different treatment of 5% $Cu_1Ni_1/SiO_2$ catalysts. Asis-catalysts were air-exposed prior to measurements.

### 3.2. In situ XRD

The changes of the Cu–Ni bimetallic nanostructure during $H_2$ reduction of the asis- and the calc-CuNi catalysts were traced with in situ XRD analysis using a synchrotron light source. Fig. 2(a) reveals no obvious diffraction signal from the asis-CuNi in the range covering reduced metals (43.3° for Cu(1 1 1) and 44.5° for Ni(1 1 1)) and metal oxides (38.7° for CuO(1 1 1), 42.3° for Cu$_2$O(2 0 0), and 43.3° for NiO(2 0 0)). A broad band close to that of Cu(1 1 1) appeared when the sample was heated incrementally under $H_2$ to 350 °C. When the temperature increased further under $H_2$ flow, the diffraction peak became more intense. The diffraction peak under $H_2$ from 350 to 650 °C was positioned between Cu(1 1 1) at 43.3° and Ni(1 1 1) at 44.5°. This indicates the formation of fcc CuNi alloy. No diffraction line other than those from fcc crystals was detected, suggesting that other phases, if they exist, were amorphous.

The asis-CuNi catalyst after calcination at 400 °C developed CuO and NiO crystal phases, and the diffraction peak width indicated a particle size of 8.3 and 12.0 nm for CuO and NiO, respectively. Fig. 2(b) shows that CuO disappeared and the diffraction peak close to Cu(1 1 1) appeared when heated to 350 °C under $H_2$ flow. At higher temperatures under $H_2$, a band appeared with twin peaks near that of Cu(1 1 1) and Ni(1 1 1). This indicates that CuO was reduced first, and NiO disappeared later at approximately 450 °C under $H_2$. Thereafter, a Cu (or Cu-rich) phase and a Ni (or Ni-rich) phase coexisted. More homogeneous alloy phase formed after 650 °C reduction.

### 3.3. XANES and EXAFS analysis

Fig. 3 shows the in situ XANES spectra of the asis-CuNi and the calc-CuNi. Fig. 3(a) shows that the asis-CuNi catalyst had a pre-edge transition like Cu metal, and a near-edge feature like a mixture of Cu

**Table 1**
$H_2$ consumption[a] at different temperature range during TPR of different catalysts.

| Catalyst | 50–250 °C | 250–450 °C | 450–800 °C | Total |
|---|---|---|---|---|
| Asis-Cu | 140 (42%) | 149 (45%) | 41 (12%) | 330 |
| Asis-CuNi | 86 (27%) | 101 (31%) | 135 (42%) | 322 |
| Calc-CuNi | 234 (48%) | 122 (25%) | 137 (28%) | 493 |
| Asis-Ni | 9 (2%) | 112 (23%) | 375 (76%) | 496 |

[a] The $H_2$ consumption is expressed in μmol/g catalyst. The percentages in parentheses represent the fractions within the total $H_2$ consumption of a catalyst sample.
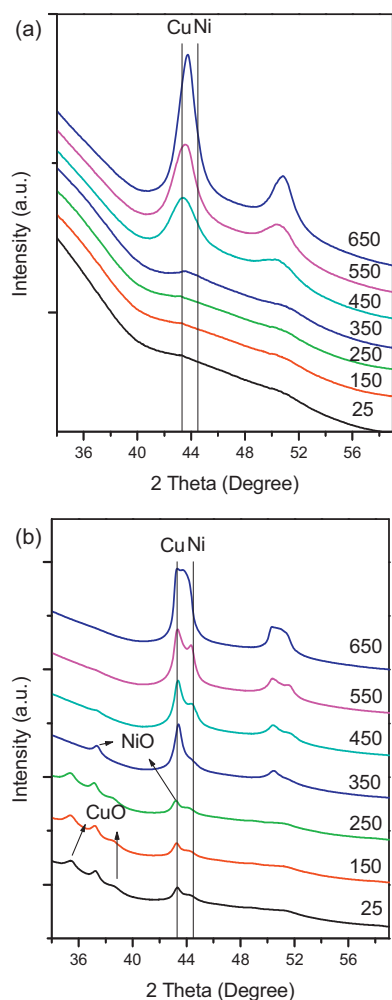
**Fig. 2.** In situ XRD patterns of (a) asis- and (b) calc-5% $Cu_1Ni_1/SiO_2$ catalysts during stepwise increase in temperature under $H_2$ atmosphere. The vertical lines indicate Cu and Ni of the $2\theta$ position at 43.3° and 44.5°, respectively.

metal and CuO. These results suggest that nano-size metal particles have an oxidized surface layer. The pre-edge transition intensity increased after pretreatment with $H_2$ at different temperatures. The asis-CuNi-R350 and the asis-CuNi-R650 catalysts exhibited XANES features similar to that of Cu metal, but the pre-edge transition intensity was more intense than that of Cu metal. This suggests a lower Cu 3d band electron density resulting from the alloy formation with Ni (Fig. 2). Fig. 3(b) shows that the Ni K-edge XANES of asis-CuNi is close to that of NiO, but the small pre-edge transition indicates the presence of the metal phase. This is consistent with the proposed CuNi alloy phase of the asis-CuNi catalyst, although a large fraction of Ni might be present in the oxidized phase. When heated under $H_2$ flow, the Ni oxide phases were partially reduced at 350 °C and completely reduced at 650 °C. Compared to the in situ XRD in Fig. 2, this suggests that the reduced Ni mixed well with Cu metal, forming an alloy.

Fig. 3(c) shows that the Cu K-edge XANES of calc-CuNi was close to that of CuO. The XANES feature remained unchanged after pretreatment in $H_2$ at 200 °C. At a reduction temperature of 350 or 650 °C, the XANES features were similar to that of Cu metal. The pre-edge transition intensities of calc-CuNi-R350 and calc-CuNi-R650 were slightly more intense than that of Cu metal, attributable to alloy formation. The Ni K-edge XANES of calc-CuNi was almost the same as that of the NiO reference, but the post-edge oscillation was somewhat different. This implies that the Ni morphology of

calc-CuNi was mainly oxidized form but somewhat different from NiO structure. $H_2$-reduction at 200 °C did not change the Ni morphology. Fig. 3(d) shows that Ni was partially reduced in calc-CuNi-R350 and was completely reduced in calc-CuNi-R650.

Fig. 4 presents the Fourier-transformed EXAFS spectra of the asis-CuNi and the calc-CuNi catalysts, and Table 2 lists the fitting results. The asis-CuNi catalyst had Cu—O and Cu—Cu metal bonds at 1.9 and 2.5 Å, respectively. The coordination numbers of these two shells were 1.9 and 3.2, respectively, indicating very small metal particles. From Ni K-edge, the asis-CuNi catalyst contained oxidized phase with peaks at approximately 2.0 Å and 3.1 Å corresponding to Ni—O and 2nd-shell Ni—Ni coordination in oxidized Ni, respectively. The Ni—Ni coordination near 3.10 Å can be attributed to $Ni(OH)_2$ [37,38] or Ni silicate [39]. It is not possible to differentiate Cu from Ni backscatters in EXAFS. It was difficult to include the Ni—Ni metallic coordination in the fitting model, although XANES indicated its presence. The absence of Ni—Ni metal bonds may be because only a part of the Ni formed alloy and the other major part was Ni oxide phase, as indicated in TPR (Fig. 1). Another reason for the absence of Ni—Ni metal coordination could be that Ni was enriched on the surface of alloy nanoparticles and became oxidized upon air exposure. This is consistent with the EXAFS data discussed below. This suggests that the asis-CuNi catalyst contains highly dispersed bimetal particles with an oxidized surface shell and some Ni oxide phase.

When asis-CuNi was reduced by $H_2$ at 200 °C, the reduced Ni phase appeared and Cu—Cu coordination increased. This supports the theory of alloy nanoparticles with surface enriched Ni. When the $H_2$-reduction temperature increased to 350 °C, the Cu—O bond disappeared completely and the coordination number of metallic Cu—Cu and Ni—Ni increased. This suggests that surface oxide was completely removed and the remaining oxidized Ni is attributable to a separated Ni oxide phase (NiO or Ni silicate). At a reduction temperature of 650 °C, only metallic Cu—Cu and Ni—Ni phase appeared, and the coordination numbers were 10.7 and 9.1, respectively. These results indicate sintered alloy particles.

Table 2 shows that the calc-CuNi catalyst contained Cu—O, 2nd-shell Cu—Cu, Ni—O and 2nd-shell Ni—Ni coordinations. This is in consistent with the presence of CuO and NiO shown in XRD (Fig. 2). The Cu—O bond at 1.95 Å shortened to 1.90 Å by $H_2$ reduction at 200 °C. The 2nd-shell Cu—Cu simultaneously shortened and metallic Cu—Cu bonds appeared, whereas Ni remained oxidized. Increasing the $H_2$-reduction temperature to 350 °C caused the disappearance of Cu—O and the emergence of reduced Ni. Reduced and oxidized phases of Ni coexisted at this condition, implying that part of the Ni oxide was in close proximity to Cu. After reduction at 650 °C, only Cu—Cu and Ni—Ni metal phases appeared with coordination numbers of 10.3 and 9.3, respectively. These coordination numbers are similar to those of asis-CuNi-R650, but the asymmetric XRD peak shape of calc-CuNi-R650 (Fig. 2) suggests the presence of two phases while that of asis-CuNi-R650 suggests a homogeneous metal mixing.

### 3.4. ESR over asis-CuNi and calc-CuNi catalysts

This section compares the ESR reaction over four catalysts, asis-CuNi-R350, asis-CuNi-R650, calc-CuNi-R350, and calc-CuNi-R650, to determine the influence of their nanostructures on reaction performance. The previous discussion shows that asis-CuNi-R650 catalyst contained sintered homogeneous CuNi alloy particles, while asis-CuNi-R350 catalyst had Cu-rich alloy bimetal particles and nearby oxidized Ni phase with support interaction. However, calc-CuNi-R350 had Cu (or Cu-rich) metal particles surrounded with oxidized Ni. The calc-CuNi-R650 catalyst contained mixed phases of Cu-rich and Ni-rich bimetal particles. The ESR reaction products of all four catalysts included only acetaldehyde, methane, CO, $CO_2$, and $H_2$. Using the method reported earlier [11], we were
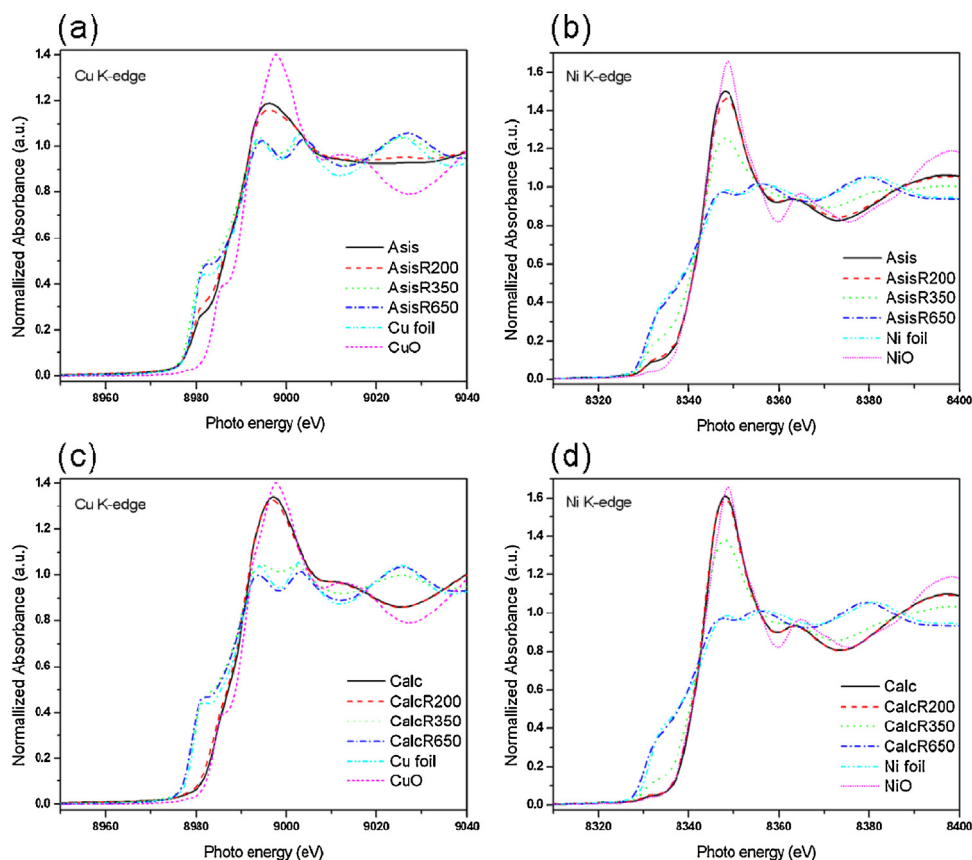
**Fig. 3.** Cu K-edge of (a, c) and Ni K-edge (b, d) XANES analysis of asis- (a, b) and calc- (c, d) 5% $Cu_1Ni_1/SiO_2$ Catalysts.

**Table 2**
Results of EXAFS model fitting of differently treated $CuNi/SiO_2$ catalysts.

| Catalyst | Shell | $R$ (Å) | Coordination number | $\sigma^2 \times 10^3$ | $E_o$ | $r$-Factor |
|---|---|---|---|---|---|---|
| Asis | Cu–O | $1.905 \pm 0.016$ | $1.9 \pm 0.5$ | $3.3 \pm 2.9$ | $6.4 \pm 2.2$ | 0.007 |
| | Cu–Cu | $2.536 \pm 0.013$ | $3.2 \pm 0.7$ | $7.2 \pm 1.8$ | | |
| | Ni–O | $2.045 \pm 0.011$ | $3.1 \pm 0.5$ | $3.1 \pm 1.7$ | $-4.7 \pm 1.5$ | 0.015 |
| | Ni–Ni | $3.089 \pm 0.018$ | $5.6 \pm 1.9$ | $15.7 \pm 3.9$ | | |
| AsisR200 | Cu–O | $1.997 \pm 0.023$ | $3.1 \pm 0.4$ | $6.0 \pm 1.9$ | $12.7 \pm 3.0$ | 0.013 |
| | Cu–Cu | $2.579 \pm 0.021$ | $6.8 \pm 0.5$ | $9.1 \pm 2.3$ | | |
| | Ni–O | $2.058 \pm 0.038$ | $4.6 \pm 1.9$ | $9.5 \pm 4.9$ | $-3.9 \pm 3.3$ | 0.007 |
| | Ni–Ni | $2.515 \pm 0.032$ | $1.9 \pm 3.2$ | $9.6 \pm 13.4$ | | |
| | Ni–Ni | $3.094 \pm 0.032$ | $2.4 \pm 2.0$ | $7.4 \pm 6.3$ | | |
| AsisR350 | Cu–Cu | $2.516 \pm 0.010$ | $8.9 \pm 1.4$ | $9.5 \pm 1.3$ | $3.6 \pm 1.6$ | 0.003 |
| | Ni–O | $2.035 \pm 0.055$ | $2.4 \pm 2.2$ | $7.2 \pm 11.6$ | $-4.4 \pm 4.2$ | 0.005 |
| | Ni–Ni | $2.511 \pm 0.027$ | $4.3 \pm 2.7$ | $6.2 \pm 4.5$ | | |
| | Ni–Ni | $3.082 \pm 0.063$ | $2.1 \pm 4.3$ | $10.3 \pm 18.3$ | | |
| AsisR650 | Cu–Cu | $2.513 \pm 0.007$ | $10.7 \pm 1.2$ | $9.5 \pm 0.9$ | $3.8 \pm 1.2$ | 0.001 |
| | Ni–Ni | $2.499 \pm 0.009$ | $9.1 \pm 1.3$ | $6.5 \pm 1.2$ | $6.5 \pm 1.6$ | 0.001 |
| Calc | Cu–O | $1.953 \pm 0.022$ | $3.1 \pm 0.4$ | $5.0 \pm 1.5$ | $-0.4 \pm 1.8$ | 0.007 |
| | Cu–Cu | $2.958 \pm 0.011$ | $4.9 \pm 2.9$ | $19.1 \pm 6.8$ | | |
| | Ni–O | $2.049 \pm 0.009$ | $5.3 \pm 0.8$ | $8.2 \pm 1.9$ | $-5.5 \pm 1.2$ | 0.007 |
| | Ni–Ni | $3.037 \pm 0.014$ | $7.9 \pm 2.0$ | $18.3 \pm 3.2$ | | |
| CalcR200 | Cu–O | $1.909 \pm 0.008$ | $2.7 \pm 0.3$ | $3.1 \pm 1.1$ | $-3.5 \pm 1.5$ | 0.002 |
| | Cu–Cu | $2.559 \pm 0.022$ | $1.4 \pm 1.7$ | $10.8 \pm 7.5$ | | |
| | Cu–Cu | $2.891 \pm 0.029$ | $1.0 \pm 1.0$ | $18.6 \pm 10.0$ | | |
| | Ni–O | $2.042 \pm 0.006$ | $4.7 \pm 0.5$ | $6.3 \pm 1.2$ | $-5.5 \pm 0.9$ | 0.003 |
| | Ni–Ni | $3.029 \pm 0.010$ | $7.8 \pm 1.4$ | $17.9 \pm 2.2$ | | |
| CalcR350 | Cu–Cu | $2.537 \pm 0.009$ | $8.1 \pm 1.0$ | $10.1 \pm 1.1$ | $-12.1 \pm 1.6$ | 0.004 |
| | Ni–O | $2.060 \pm 0.055$ | $4.2 \pm 2.5$ | $9.7 \pm 7.7$ | $-5.7 \pm 5.3$ | 0.011 |
| | Ni–Ni | $2.523 \pm 0.034$ | $3.4 \pm 3.1$ | $8.6 \pm 7.3$ | | |
| | Ni–Ni | $3.092 \pm 0.066$ | $2.7 \pm 4.3$ | $12.5 \pm 14.2$ | | |
| CalcR650 | Cu–Cu | $2.532 \pm 0.009$ | $10.3 \pm 1.4$ | $8.8 \pm 1.2$ | $-10.6 \pm 1.6$ | 0.001 |
| | Ni–Ni | $2.503 \pm 0.034$ | $9.3 \pm 1.0$ | $6.1 \pm 0.9$ | $-10.9 \pm 1.3$ | 0.001 |

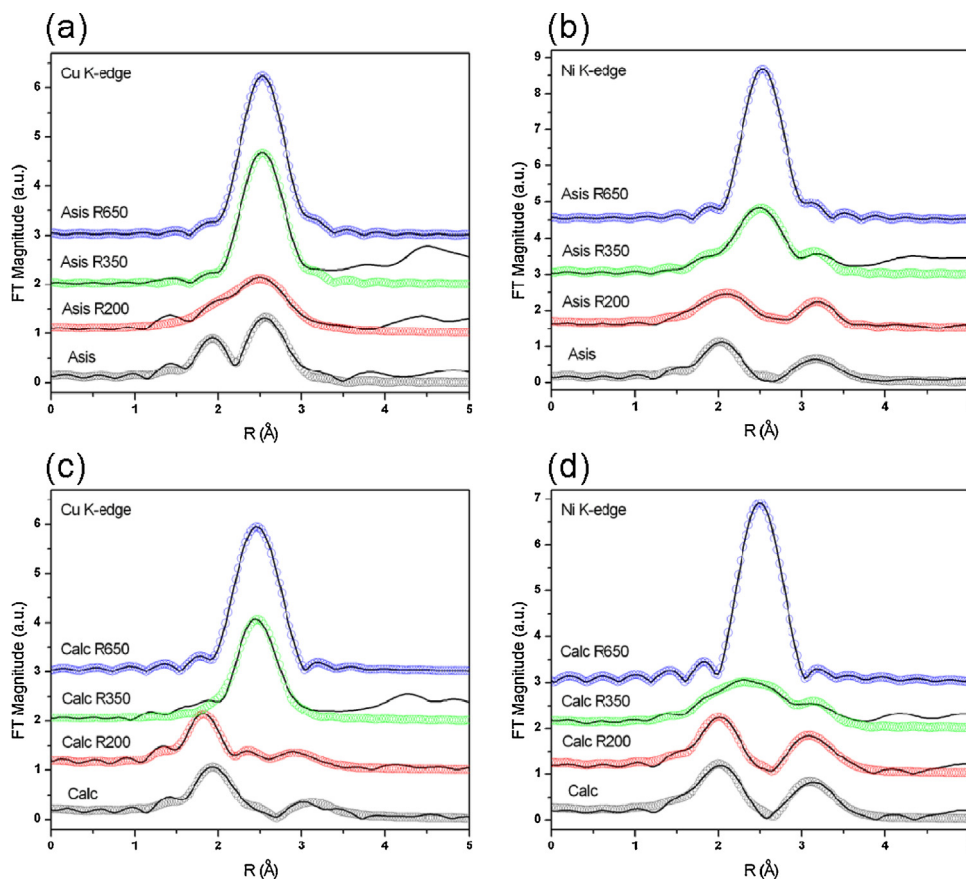**Fig. 4.** Cu K-edge of (a, c) and Ni K-edge of (b, d) EXAFS analysis of asis- (a, b) and calc- (c, d) 5% $Cu_1Ni_1/SiO_2$ Catalysts. Lines represent experimental data and symbols represent fittings using models presented in Table 2.

able to calculate as a function of reaction temperature the fractional conversion of acetaldehyde, the selectivity of acetaldehyde steam reforming (ASR), the fractional CO conversion via water gas shift (WGS), and the $H_2$ yield. All values were based on per mole of EtOH converted. The SRE reaction performance of different catalysts was compared based on these results.

Fig. 5 compares the ESR performance for all four $CuNi/SiO_2$ catalysts under identical test conditions. Kinetic data of ESR over the two more active catalysts will be reported below. Fig. 5(a) shows that the calc-CuNi catalysts were more active than the asis-CuNi catalysts and the 650 °C-reduced catalysts were less active than the 350 °C-reduced catalysts. The very different EtOH conversions under identical test conditions imply that the data are not subjected to significant mass transfer limitation. The most active calc-CuNi-R350 catalyst completely converted EtOH at 300 °C. The hydrogen yields (Fig. 5(b)) were all slightly larger than 1 at temperatures below 350 °C, indicating the primary formation of acetaldehyde. At higher temperatures, the hydrogen yield increased with temperature, and the calc-CuNi-R350 catalyst had the fastest rise in hydrogen yield.

Fig. 5(c) shows the acetaldehyde conversion per mole of converted EtOH. The calc-CuNi-R350 catalyst had the highest fractional conversion of acetaldehyde, indicating the best activity for breaking C—C bonds during ESR. Fig. 5(d) shows the calculated ASR selectivity when acetaldehyde was converted. ASR is preferable to the competing acetaldehyde decomposition (AD) because the latter produces $CH_4$ and consequently decreases $H_2$ yield. A higher reaction temperature resulted in higher ASR selectivity. The 350 °C-reduced catalysts had higher ASR selectivity than the 650 °C-reduced catalysts. This implies that sintered metal particles promoted AD

compared to small particles. The calc-CuNi-R350 catalyst showed higher ASR selectivity than the asis-CuNi-R350 catalyst, consistent with the higher hydrogen yield of the former catalyst (Fig. 5(b)). However, the ASR selectivity of calc-CuNi-R350 was below 0.3 at temperatures below 350 °C. This ASR selectivity should be improved further to increase $H_2$ yield.

Fig. 5(e) shows the calculated CO fractional conversion via WGS per mole of converted EtOH, which started only at temperatures above 300 °C. The calc-CuNi catalysts had higher CO conversion than the asis-CuNi catalysts. The reduction temperature did not change the CO conversion of the calc-catalysts, but the asis-CuNi-R650 had much lower CO conversion than asis-CuNi-R350 catalyst. This suggests that mixed-phase morphology favors WGS. Fig. 5(d) and (e) indicate that the calc-CuNi catalysts promoted the water-involved reaction pathways (i.e., ASR and WGS).

Fig. 5(f) compares the tendency of coke formation in terms of the carbon mole balance of the reactor effluent. The carbon balance of effluent was mostly within 95% of the feed at temperatures below 350 °C for all catalysts, indicating that the extent of coking was insignificant. Coke started to form at higher temperatures. The increase in coke formation seems to occur at the same time the hydrogen yield increased (Fig. 5(b)). This suggests that C—C bond breaking during ESR leads to both $H_2$ formation and coke formation. The calc-CuNi-R350 catalyst had the highest $H_2$ yield and acetaldehyde conversion, and a lower tendency of coke formation than the other three catalysts during SRE reaction. Thermogravimetry analysis (TGA) of spent catalysts revealed the same trend in coking tendency. The results of TGA indicate a weight loss of 12.5 and 4.5 wt% (on dry basis) respectively in the burn-off of spent asis-CuNi-R350 and calc-CuNi-R350.
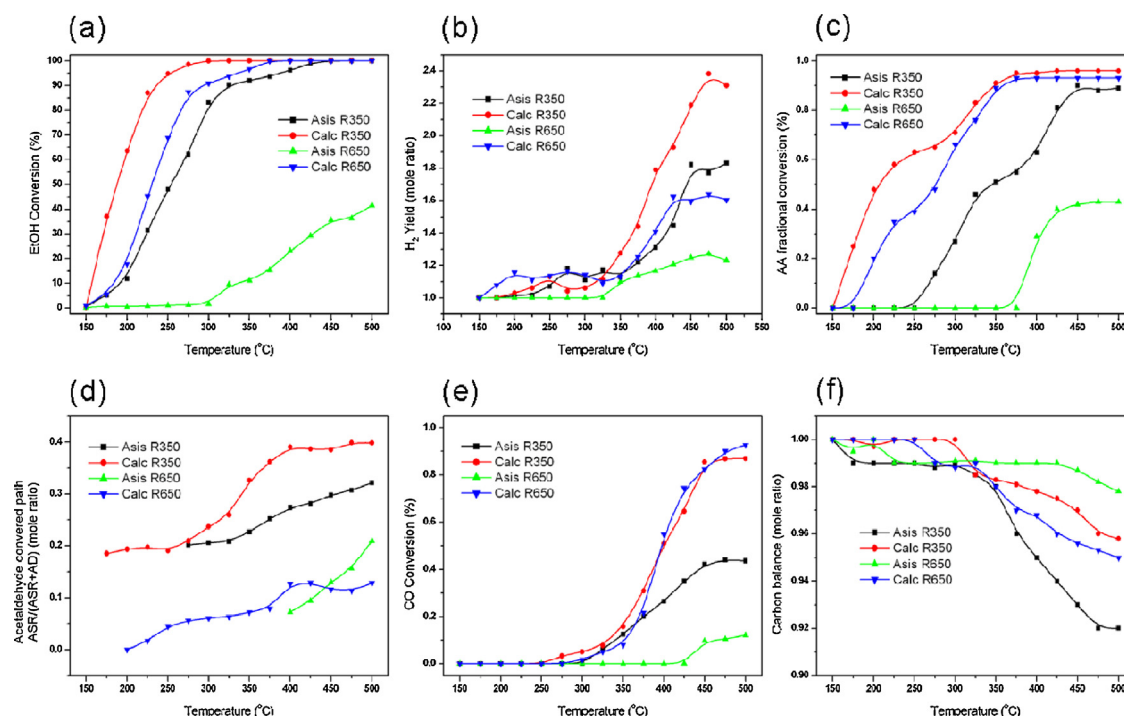
**Fig. 5.** (a) The ethanol conversion and (b) the $H_2$ yield (c) the calculated acetaldehyde fractional conversion (d) the calculated acetaldehyde selectivity (e) the calculated CO fractional conversion and (f) the effluent C-balance on 5% $Cu_1Ni_1/SiO_2$ during temperature-programmed SRE tests. The missing carbon in effluent C-balance is considered an index of coking tendency. The tests were carried out at $H_2O/EtOH = 6$, WHSV = 2 g EtOH/g cat h, and 1 K/min.

Kinetic data of ESR and of ASR over the two more active catalysts, i.e., asis-CuNi-R350 and calc-CuNi-R350 were recorded at isothermal steady state under differential reactor conditions. The TOFs (turnover frequency), based on $M_S$ analyzed by $N_2O$ adsorption, are compared in Fig. 6 and Table 3. Under the test conditions, ESR produced only $H_2$ and AA (acetaldehyde) indicating ethanol dehydrogenation (when the reaction was performed with S/E = 6) while the products from ASR contained $H_2$, CO, and $CH_4$. Fig. 6(a) shows that calc-CuNi-R350 had higher TOF and lower activation energy for ethanol dehydrogenation than asis-CuNi-R350. At 200 °C, the ethanol dehydrogenation TOF of calc-CuNi-R350 is around two times that of asis-CuNi-R350. The specific activity of acetaldehyde was also examined with a feed of steam/AA = 6. Calc-CuNi-R350 showed orders of magnitude higher TOF for acetaldehyde conversions than asis-CuNi-R350. Based on the product distribution of $H_2$, $CH_4$ and CO, we calculated the fractional conversions of AA via AD and via ASR and their TOFs are shown in Fig. 6(b). The AD was the preferred reaction pathway for both catalysts. The apparent activation energy of AD, ASR, and overall AA conversion were similar over the two catalysts. At 10% AA conversion (Table 3), the ratio $TOF_{AD}/TOF_{ASR}$ over calc-CuNi-R350 and asis-CuNi-R350 was 3.5 and 4.3 respectively, and $T_{10}$ (the temperature when 10% conversion was achieved) over calc-CuNi-R350 and asis-CuNi-R350 was 175 and 275 °C respectively. This clearly indicates that calc-CuNi-R350 has a much higher specific activity for AA conversion and a higher selectivity for ASR than asis-CuNi-R350.

Table 4 summarizes the kinetic activity and the product selectivity of ESR over these CuNi catalysts (Figs. 5 and 6) and the monometallic catalysts prepared by the same procedures. At 300 °C, both the Cu catalyst and the Ni catalyst had a lower TOF of EtOH conversion than bimetallic CuNi catalysts. Neither of them catalyzed the conversion of AA; Cu is known to be lack of the activity to break C—C bond and the Ni catalyst had low activity to break C—C bond at 300 °C. The advantages of using bimetallic CuNi catalysts include high TOF for ethanol conversion and also the ability to catalyze AA conversion to $H_2$, CO and $CH_4$. Table 4 shows that the calc-CuNi-R350 catalyst is superior to asis-CuNi-R350 and $CuNi/CeO_2$ reported in [26] in its higher TOF for ethanol conversion, higher AA conversion activity, and higher ASR/AD selectivity. The ESR at $H_2O/EtOH = 3$ over $3\%Pt10\%Ni/CeO_2$ [32] produced a significantly higher selectivity to $CH_4$ than calc-CuNi-R350 when both catalysts resulted in 100% EtOH conversion at 350 °C. The formation of $CH_4$ from a secondary methanation reaction is indicated at long contact time ESR condition over this $3\%Pt10\%Ni/CeO_2$ catalyst

**Table 3**

The TOF (turnover frequency) and activation energy ($E_a$) of ESR and ASR over differently treated $CuNi/SiO_2$ catalysts.

| Reaction | Activity @ 10% conversion | | | | Activation energy | |
|---|---|---|---|---|---|---|
| | Asis-R350 | | Calc-R350 | | Asis-R350 | Calc-R350 |
| | $T_{10}$ (°C) | TOF ($s^{-1}$) | $T_{10}$ (°C) | TOF ($s^{-1}$) | $E_a$ (kJ/mol) | $E_a$ (kJ/mol) |
| ESR[a] | 200 | 0.0063 | 170 | 0.0062 | 64 ± 16 | 52 ± 1 |
| ASR[b] | 275 | 0.0053 | 175 | 0.0059 | 69 ± 5 | 63 ± 7 |
| AA → $CH_4$ + CO | 275 | 0.0043 | 175 | 0.0046 | 68 ± 5 | 62 ± 7 |
| AA + $H_2O$ → 2CO + $3H_2$ | 275 | 0.0010 | 175 | 0.0013 | 72 ± 4 | 68 ± 7 |

[a] The observed products from ESR contained $H_2$ and acetaldehyde, indicating that only ethanol dehydrogenation occurred under the reaction conditions used.

[b] The observed products from ASR contained $H_2$, CO, and $CH_4$. Based on the product distribution, the overall acetaldehyde conversion was distinguished into the fractional conversions of acetaldehyde decomposition and that of acetaldehyde steam reforming and then the TOFs were calculated respectively.

**Table 4**
Comparison of the ESR catalytic performance of different catalysts.

| Catalyst | $D^a$ (%) | $X_{EtOH}$ (%) | $TOF_{EtOH}^b$ (1/s) | C-product distribution[c] | | | | $S_{ASR/AD}^d$ |
|---|---|---|---|---|---|---|---|---|
| | | | | AA | $CH_4$ | CO | $CO_2$ | |
| @300 °C | | | | | | | | |
| Cu-R350 | 15.6 | 57.4 | (0.047) | 1.00 | – | – | – | – |
| Ni-R350 | 1.9 | 14.2 | 0.012 | 1.00 | – | – | – | – |
| Asis-CuNi-R350 | 22.9 | 83.2 | 0.099+ | 0.68 | 0.12 | 0.20 | – | 0.26 |
| Asis-CuNi-R650 | 2.8 | 1.6 | 0.007 | 1.00 | – | – | – | – |
| Calc-CuNi-R350 | 22.0 | 100 | 0.144+ | 0.15 | 0.32 | 0.51 | 0.03 | 0.31 |
| Calc-CuNi-R650 | 5.4 | 91.0 | (0.206) | 0.19 | 0.38 | 0.42 | 0.01 | 0.06 |
| @350 °C | | | | | | | | |
| Asis-CuNi-R350 | 22.9 | 92.1 | 0.277+ | 0.31 | 0.27 | 0.36 | 0.05 | 0.29 |
| Calc-CuNi-R350 | 22.0 | 100 | 0.343+ | 0.06 | 0.29 | 0.55 | 0.10 | 0.48 |
| 10%$Cu_{1.5}Ni_{98.5}$/$CeO_2^e$ | 14.9 | 38.2 | (0.031) | 0.45 | 0.29 | 0.14 | 0.12 | – |
| 15%$Cu_{1.5}Ni_{98.5}$/$CeO_2^e$ | 7.1 | 40.6 | (0.046) | 0.41 | 0.34 | 0.14 | 0.11 | – |
| 3%Pt10%Ni/$CeO_2^f$ | – | 100 | – | Nil | 0.62 | 0.02 | 0.36 | – |

[a] The metal dispersion analyzed by the $N_2O$ adsorption method.
[b] $TOF_{EtOH}$, calculated from the EtOH conversion and a differential reactor equation. Numbers in parentheses indicates the calculation from the data with EtOH conversion higher than differential reaction condition. A "+" sign is used to mark those calculated from the extrapolation of data in Fig. 6.
[c] Carbon-product distribution in mole fraction.
[d] $S_{ASR/AD}$, the calculated selectivity of ASR over the selectivity of AD, based on the product distribution and the method reported in [11].
[e] Data from [26], where the ESR tests were at $H_2O$/EtOH = 7.6 mol, WHSV = 3.16 g EtOH/g catalyst h, or $1.9 \times 10^{-5}$ gmol EtOH/g catalyst s. In comparison, the ESR tests of this study were at $H_2O$/EtOH = 6 mol, WHSV = 2 g EtOH/g catalyst h, or $1 \times 10^{-5}$ gmol EtOH/g catalyst s.
[f] Data from [32], where the ESR tests were at $H_2O$/EtOH = 3 mol , GHSV = 15,000 $h^{-1}$, $P_{EtOH}$ = 5 kPa.
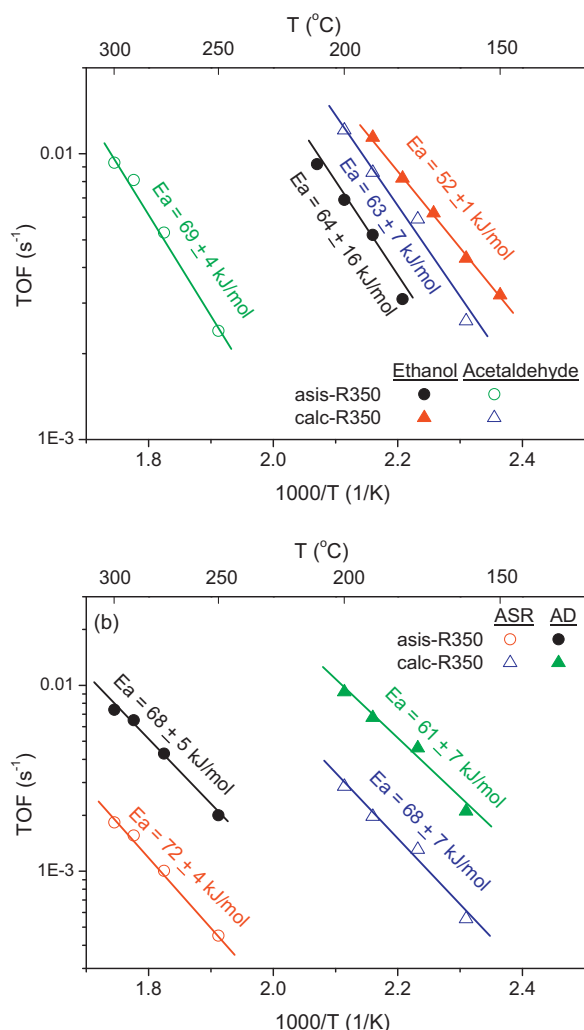


**Fig. 6.** Arrhenius plot of (a) the TOF (turnover frequency) of ESR and ASR (acetaldehyde steam) reaction over asis-CuNi-R350 and calc-CuNi-R350 catalysts, and (b) the breakdown TOF of AD and ASR reaction pathway during ASR. The kinetic tests were measured with $H_2O$/EtOH(AA) = 6 under isothermal steady state condition. TOF was calculated based on the exposed metal surface analyzed by $N_2O$ adsorption.

[31]. However, the comparison cannot be unequivocal because of their differences in space velocity and in steam ratio. Nonetheless, comparison between asis-CuNi-R350 and calc-CuNi-R350 clearly indicates that the morphology of metal nanoparticles surrounded with oxidized Ni in calc-CuNi-R350 had high kinetic activity for ESR and ASR.

### 3.5. Effect of S/E (steam/EtOH) ratio

Fig. 5 and Table 4 suggest that the calc-CuNi-R350 catalyst promoted the water-involved reaction pathways (ASR and WGS). Fig. 7 shows the SRE results for the influence of increasing the S/E ratio from 6 to 9 over asis-CuNi-R350 and calc-CuNi-R350. When the S/E ratio increased, the ethanol conversions over calc-CuNi-R350 increased only slightly (Fig. 7(a)) but the $H_2$ yield increased significantly. The calculated acetaldehyde conversion decreased as the S/E ratio increased at low temperatures (Fig. 7(c)), but the ASR selectivity increased (Fig. 7(d)). This increase in $H_2$ yield is the result of suppressed AD activity by the increased S/E ratio. The CO fractional conversion slightly increased (Fig. 7(e)) and the coking was furthered suppressed by the increase of the S/E ratio. This supports the claimed enhancement in the water-participated reaction pathways of ASR and WGS.

The increase of the S/E ratio from 6 to 9 significantly improved EtOH conversions for asis-CuNi-R350 (Fig. 7(a)), and the $H_2$ yield also increased significantly (Fig. 7(b)). However, the ASR selectivity did not change (Fig. 7(d)). This indicates that the increased $H_2$ yield is due to the promoted ethanol and acetaldehyde conversions (Fig. 7(c)). The CO fractional conversion over asis-CuNi-R350 became slightly lower when S/E increased, indicating that an increased S/E ratio did not enhance WGS. The increase of $H_2$ yield over the asis-CuNi-R350 by the increased S/E ratio is likely the result of increased conversions, but the reaction pathway selectivity was not influenced. The coking tendency on both catalysts decreased when the S/E ratio increased.

### 4. Discussion

For ESR reaction, Ni has high activity for C—C bond breaking, O—H bond breaking [9], hydrogenation, and helping H atoms form molecular $H_2$ [40]. However, coke formation started at temperatures below 400 °C when using a monometallic Ni catalyst prepared
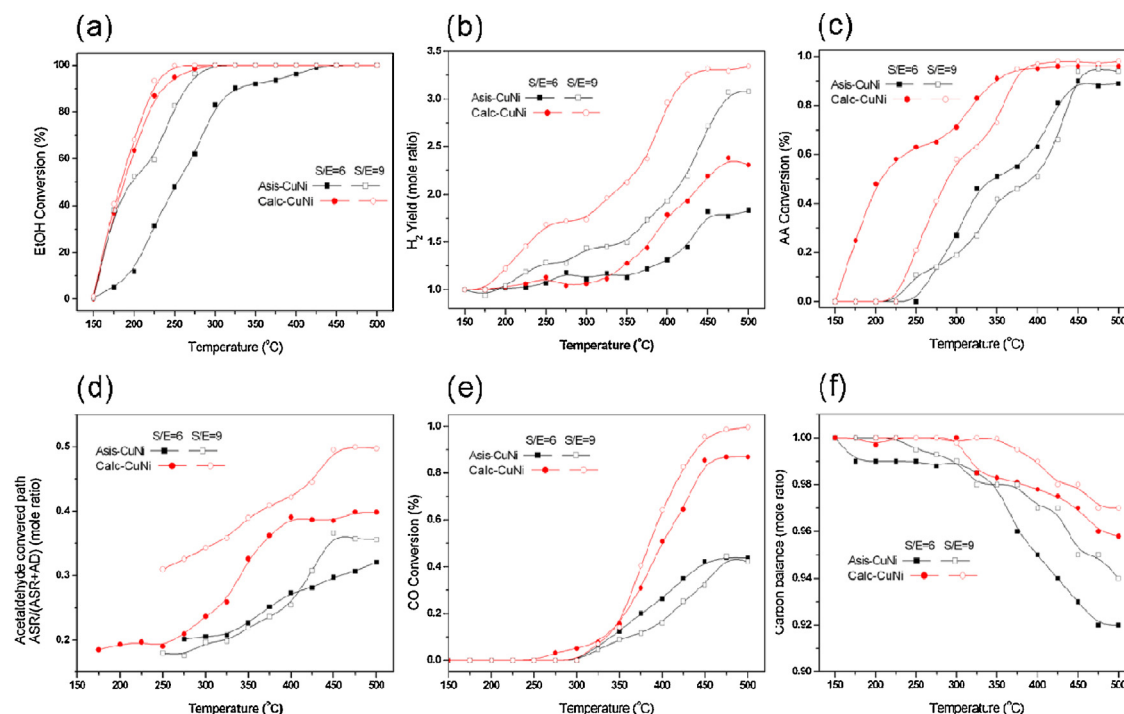
**Fig. 7.** Effect of increasing S/E from 6 to 9 on (a) the ethanol conversion and (b) the $H_2$ yield (c) the calculated acetaldehyde fractional conversion (d) the calculated acetaldehyde selectivity (e) the calculated CO fractional conversion and (f) the coking index by C-balance on the 5% $Cu_1Ni_1/SiO_2$ reduced in $H_2$ at 350 °C during temperature-programmed SRE tests. The tests were carried out at $H_2O/EtOH = 6$ or 9, WHSV = 2 g EtOH/g cat h, and 1 K/min.

and tested as in this study. Several reports [41–44] have mentioned a similarly high coking tendency for Ni catalysts in ESR. A monometallic Cu catalyst is only effective for EtOH dehydrogenation to produce acetaldehyde [3,9,44,45]. This indicates that it is ineffective in breaking C—C bonds, which is a necessary step in ESR. Bimetallic Cu–Ni catalysts were found capable of breaking C—C bonds [8–17,25,46]. The extent of coking in bimetallic Cu–Ni during ESR can be largely suppressed by using Cu/Ni ≥ 1 and the preparation method reported in this study. However, the Ni-rich bimetallic CuNi catalysts still have a high coking tendency [11].

The reaction pathway in Scheme 1 can improve the efficiency of $H_2$ production with ESR because it produces only simple C1 side products of CO, $CO_2$, and $CH_4$. Mariño et al. [9] proposed that ESR at a temperature below 400 °C is a practical approach even when $CH_4$ constitutes a part of production gas. Palma and co-workers [29–32] also emphasize that decreasing the reaction temperature of ESR can lead to more efficient $H_2$ production. However, our previous research [11] has demonstrated that $CH_4$ dehydrogenation resulted in coke formation over CuNi/SiO$_2$ at temperatures below 400 °C, especially the Ni-rich catalysts. This study demonstrates that calc-CuNi-R350 had a lower selectivity to $CH_4$ formation (i.e., a higher ASR/AD selectivity) than asis-CuNi-R350. This indicates that the suppression of $CH_4$ formation may be possible with the appropriate morphology of bimetallic CuNi catalysts.

Acetaldehyde formed from EtOH dehydrogenation is generally the first intermediate product during ESR [1]. How acetaldehyde is subsequently converted determines the overall performance of ESR including the $CH_4$ formation. Transition metal surfaces decompose acetaldehyde by breaking its C—C bond. This type of acetaldehyde decomposition is frequently called decarbonylation [42,47,48], indicating the formation of methyl (or methylene) and CO (or formyl) species [3,49–52]. Further dehydrogenation of formyl and methyl groups leads to CO [50] and coke [49,53] formation, respectively. If CO is converted to $CO_2$ by WGS pathway the CO from acetaldehyde decomposition is an acceptable intermediate. This causes a paradox in ESR: the complete dehydrogenation

of acetaldehyde and $CH_4$ can provide high $H_2$ yields, but the simultaneous coke formation can deactivate the catalyst. A preferable approach for improving ESR performance should consider suppressing the dehydrogenation of methyl groups. Without further dehydrogenation, methyl groups on metal surface must combine with H to evolve $CH_4$ [54] or combine with surface oxygenates (O or OH) to form methoxy-like species. The latter route can also yield high $H_2$ in ESR if the methoxy-like species is converted in a similar way to the methoxy in MSR. Guo and Zaera showed that the methyl moieties from $CH_3I$ over Ni(1 1 0) produce $CH_4$ in the presence of surface hydrogen [55], and can form formaldehyde in the presence of surface oxygen [56]. They also observed the suppression of methyl dehydrogenation to coke in the presence of surface oxygen. Dickens and Stair [57] reported the formation of alkoxy when methyl radicals adsorbed on NiO, and that CO evolved in later temperature programmed desorption (TPD). On the other hand, acetaldehyde on oxide surfaces may form acetate without C—C bond breaking [58,59]. These results suggest that inducing active oxygen over Ni or inclusion of NiO can suppress $CH_4$ formation leading to efficient $H_2$ production from ESR.

Accordingly, the key step for high $H_2$ yield is likely the transformation of methyl groups (from acetaldehyde decomposition) to methoxy-like species which may occur with certain morphology. This study demonstrates that the morphology of bimetallic Cu-Ni catalysts has a strong influence on ESR performance. Fig. 8 summarizes the morphology changes with pretreatments from this study. The Cu-Ni catalyst after calcination became more efficient for ESR than the asis-catalysts, which implies that mixed phases can be more efficient than the homogeneous alloy phase. The asis-CuNi contains highly dispersed bimetallic particles, and CuO and NiO phases evolved after calcination. This is likely the result of a mismatch in CuO and NiO crystal lattices. This also suggests that the evolved CuO and NiO are in close proximity to each other. Consequently, calc-CuNi-R350 can develop an interface between reduced metal and NiO. This interface likely contributes to the change in
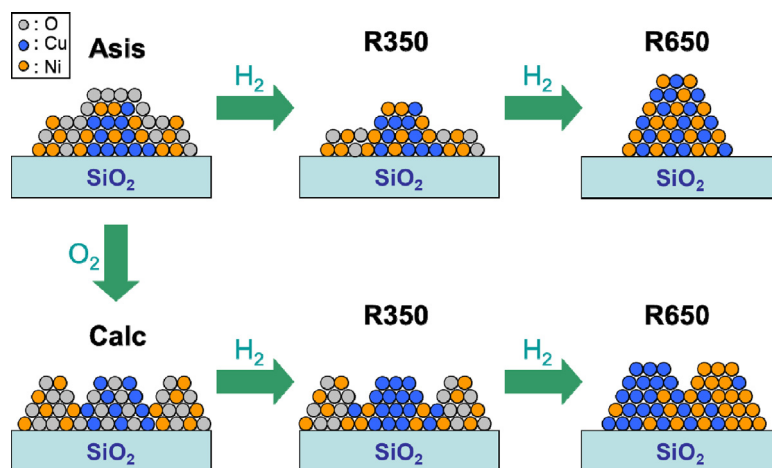
**Fig. 8.** Schematic illustration of the structural changes of the CuNi/SiO$_2$ at different stage of pretreatment.

the product selectivity of ESR, especially the selectivity between AD and ASR during C—C bond breaking. As Scheme 1 shows, AD is estimated based on the evolved CH$_4$, which can be attributed to the methyl groups with H on metal surface. ASR involves a reaction with H$_2$O, and can be considered as the reaction between OH (or surface O) and decomposed species from acetaldehyde. A higher ASR selectivity indicates that more of the decomposed species from acetaldehyde react with OH (or surface O). A hypothetical model for the higher ASR selectivity over calc-CuNi-R350 is that acetaldehyde decomposes near the metal–NiO interface and the formed methyl groups are stabilized on NiO. Methyl groups are more stable when adsorbed by the exposed oxygen on NiO than on metal surface. The acetaldehyde decomposition near the metal–NiO interface can thus produce methoxy-like species and suppress CH$_4$ evolution. The experiment of increasing the S/E ratio over calc-CuNi-R350 (Fig. 7) in this study showed that CH$_4$ suppression by the increased surface OH groups effectively increased H$_2$ yield. An increased S/E ratio also facilitates the subsequent conversion of this methoxy-like species. The CH$_4$ evolution increases again once the oxidized Ni phase is completely reduced, as that observed in calc-CuNi-R650. This indicates that the metal–oxide interface can enhance ASR selectivity and the overall performance of ESR.

Table 4 shows that the advantage of using CuNi bimetal catalysts for ESR is not just in the enhanced TOFs (for EtOH and AA), but also in an enhanced ASR selectivity which causes a change in product distribution. The presence of a Ni-rich phase, as in calc-CuNi-R650, results in a low ASR selectivity and a high coking tendency. However, the effects of Cu/Ni ratio on TOF cannot be unambiguously determined from the results of this study because the morphology changes at different stages of pretreatment (Fig. 8) even though the overall Cu/Ni is 1. Thus, the optimal Cu/Ni ratio in the reduced metal phase and the optimal metal-oxide mixed morphology of this bimetallic CuNi catalyst requires further investigation. When CH$_4$ evolution can be completely suppressed, the simple ESR reaction scheme shown in Scheme 1 becomes a very effective H$_2$ production method and the product distribution of ESR can become as simple as that in MSR.

## 5. Conclusions

The morphology of the CuNi/SiO$_2$ prepared by NaBH$_4$ reduction (the asis-CuNi sample) is changed by a further calcination (the calc-CuNi sample). The as-prepared catalyst consists of Cu-rich bimetallic alloy nanoparticles and oxidized Ni phase, which may interact with the support. After calcination, alloy nanoparticles segregate to form CuO and NiO.

The different H$_2$ reduction temperatures lead to different catalyst morphology. After 350 °C H$_2$ treatment, the surface oxide of nanoparticles in the asis-catalyst is reduced but not the oxidized Ni phase. Under the same reduction conditions, the calc-catalyst develops Cu-rich metal particles with oxidized Ni in close proximity. After H$_2$ reduction at 650 °C, all oxidized Ni is reduced; the asis-catalyst contains sintered homogeneous alloy particle and the calc-catalyst contains mixed phases of Cu-rich and Ni-rich alloy particles.

Both asis-CuNi-R650 and calc-CuNi-R650 catalysts had lower EtOH conversion during ESR than the counter catalysts reduced at 350 °C. This is attributable to the sintered particles. The presence of Cu-rich and Ni-rich mixed phases in calc-CuNi-R650 led to higher ESR performance than the homogeneous CuNi alloy phase in asis-CuNi-R650. This suggests the important role of the interface in mixed-phase morphology.

The ESR over calc-CuNi-R350 had the highest EtOH conversion, highest H$_2$ yield, highest ASR/AD selectivity, and the highest AA and CO fractional conversions among the catalysts tested in this study. When the S/E ratio increased from 6 to 9, the ASR selectivity during ESR over calc-CuNi-R350 increased. However, increasing the S/E ratio over asis-CuNi-R350 only increased the conversions, but not the ASR selectivity. This suggests that the interface between NiO and Cu-rich particles in calc-CuNi-R350 can suppress CH$_4$ evolution, and thus increase H$_2$ yield.

The calc-CuNi-R350 catalyst showed significantly higher TOFs in ESR and acetaldehyde steam reforming and a lower selectivity to CH$_4$ formation than the uncalcined but reduced catalyst (asis-CuNi-R350). Both calc-CuNi-R350 and asis-CuNi-R350 have similar metal dispersion. This suggests that the different morphology is responsible for the different ESR performance. It is attributed to the enhancement of the H$_2$O-involved reaction pathways (i.e., ASR and WGS) possibly by the interface between Cu-rich metal particles and surrounding NiO.

## References

[1] L.V. Mattos, G. Jacobs, B.H. Davis, F.B. Noronha, Chem. Rev. 112 (2012) 4094–4123.
[2] N. Bion, D. Duprez, F. Epron, ChemSusChem 5 (2012) 76–84.

[3] J.-H. Wang, C.S. Lee, M.C. Lin, J. Phys. Chem. C 113 (2009) 6681–6688.
[4] D.L. Trimm, Catal. Today 37 (1997) 233–238.
[5] D.L. Trimm, Catal. Today 49 (1999) 3–10.
[6] S.O. Choi, I.Y. Ahn, S.H. Moon, Korean J. Chem. Eng. 26 (2009) 1252–1258.
[7] V.D. Santoa, A. Gallo, A. Naldoni, M. Guidotti, R. Psaro, Catal. Today 197 (2012) 190–205.
[8] F.J. Mariño, E.G. Cerrella, S. Duhalde, M. Jobbagy, M.A. Laborde, Int. J. Hydrogen Energy 23 (1998) 1095–1101.
[9] F. Mariño, G. Baronetti, M. Jobbagy, M. Laborde, Appl. Catal. A: Gen. 238 (2003) 41–54.
[10] F. Mariño, M. Boveri, G. Baronetti, M. Laborde, Int. J. Hydrogen Energy 26 (2001) 665–668.
[11] L.-C. Chen, S.D. Lin, Appl. Catal. B: Environ. 106 (2011) 639–649.
[12] B. Lorenzut, T. Montini, L. De Rogatis, P. Canton, A. Benedetti, P. Fornasiero, Appl. Catal. B: Environ. 101 (2011) 397–408.
[13] C.N. Xian, J.G. Li, H. Li, L.Q. Chen, J. Sun, J.S. Lee, IOP Conf. Ser.: Mater. Sci. Eng. 18 (2011) 132005.
[14] L. De Rogatis, T. Montini, B. Lorenzut, P. Fornasiero, Energy Environ. Sci. 1 (2008) 501–509.
[15] V. Fierro, O. Akdim, H. Provendier, C. Mirodatos, J. Power Sources 145 (2005) 659–666.
[16] W. Wang, Int. J. Green Energy 6 (2009) 92–103.
[17] V. Fierro, O. Akdim, C. Mirodatos, Green Chem. 5 (2003) 20–24.
[18] M.H. Youn, J.G. Seo, H. Lee, Y. Bang, J.S. Chung, I.K. Song, Appl. Catal. B: Environ. 98 (2010) 57–64.
[19] A.C. Furtado, C.G. Alonso, M.P. Cantão, N.R.C. Fernandes-Machado, Int. J. Hydrogen Energy 36 (2011) 9653–9662.
[20] M.C. Sánchez-Sánchez, R.M. Navarro, J.L.G. Fierro, Int. J. Hydrogen Energy 32 (2007) 1462–1471.
[21] M.N. Barroso, A.E. Galetti, M.F. Gomez, L.A. Arrúa, M.C. Abello, Chem. Eng. J. 222 (2013) 142–149.
[22] K.-H. Lin, C.-B. Wang, S.-H. Chien, Int. J. Hydrogen Energy 38 (2013) 3226–3232.
[23] H. Muroyama, R. Nakase, T. Matsui, K. Eguchi, Int. J. Hydrogen Energy 35 (2010) 1575–1582.
[24] W. Xu, Z. Liu, A.C. Johnston-Peck, S.D. Senanayake, G. Zhou, D. Stacchiola, E.A. Stach, J.A. Rodriguez, ACS Catal. 3 (2013) 975–984.
[25] B. Prakash, K. Deepak, Int. J. Hydrogen Energy 32 (2007) 969–980.
[26] Q. Liu, Z. Liu, X. Zhou, C. Li, J. Ding, J. Rare Earths 29 (2011) 872–877.
[27] A.C. Furtado, C.G. Alonso, M.P. Cantão, N.R.C. Fernandes-Machado, Int. J. Hydrogen Energy 34 (2009) 7189–7196.
[28] G. Bonura, C. Cannilla, F. Frusteri, Appl. Catal. B: Environ. 121–122 (2012) 135–147.
[29] P. Ciambelli, V. Palma, A. Ruggiero, Appl. Catal. B: Environ. 96 (2010) 18–27.
[30] P. Ciambelli, V. Palma, A. Ruggiero, Appl. Catal. B: Environ. 96 (2010) 190–197.
[31] V. Palma, F. Castaldo, P. Ciambelli, G. Iaquaniello, G. Capitani, Int. J. Hydrogen Energy 38 (2013) 6633–6645.
[32] V. Palma, F. Castaldo, P. Ciambelli, G. Iaquaniello, Appl. Catal. B: Environ. (2013), http://dx.doi.org/10.1016/j.apcatb.2013.01.053.
[33] A. Iulianelli, A. Basile, Int. J. Hydrogen Energy 35 (2010) 3170–3177.
[34] M. Domínguez, E. Taboada, E. Molins, J. Llorca, Catal. Today 193 (2012) 101–106.
[35] E.G.M. Kuijpers, M.W.C.M.A. Nieuwesteeg, G.J. Wermer, J.W. Geus, J. Catal. 112 (1988) 107–115.
[36] J. Ashok, P.S. Reddy, G. Raju, M. Subrahmanyam, A. Venugopal, Energy Fuels 23 (2009) 5–13.
[37] O. Clause, L. Bonneviot, M. Che, H. Dexpert, J. Catal. 130 (1991) 21–28.
[38] O. Clause, B. Rebours, E. Merlen, F. Trifiró, A. Vaccari, J. Catal. 133 (1992) 231–246.
[39] M. Richard-Plouet, M. Guillot, A. Traverse, D. Chateigner, S. Vilminot, Nucl. Instr. Meth. Phys. Res. B 200 (2003) 148–154.
[40] J. Kugai, S. Velu, C. Song, Catal. Lett. 101 (2005) 255–264.
[41] A. Denis, W. Grzegorczyk, W. Gac, A. Machocki, Catal. Today 137 (2008) 453–459.
[42] A.J. Vizcaíno, P. Arena, G. Baronetti, A. Carrero, J.A. Calles, M.A. Laborde, N. Amadeo, Int. J. Hydrogen Energy 33 (2008) 3489–3492.
[43] A.N. Fatsikostas, X.E. Verykios, J. Catal. 225 (2004) 439–452.
[44] A.J. Vizcaíno, A. Carrero, J.A. Calles, Int. J. Hydrogen Energy 32 (2007) 1450–1461.
[45] M. Bowker, R.J. Madix, Surf. Sci. 116 (1982) 549–572.
[46] V. Klouz, V. Fierro, P. Denton, H. Katz, J.P. Lisse, S. Bouvot-Mauduit, C. Mirodatos, J. Power Sources 105 (2002) 26–34.
[47] S. Cavallaro, Energy Fuels 14 (2000) 1195–1199.
[48] J. Comas, F. Marino, M. Laborde, N. Amadeo, Chem. Eng. J. 98 (2004) 61–68.
[49] A.F. Lee, D.E. Gawthrope, N.J. Hart, K. Wilson, Surf. Sci. 548 (2004) 200–208.
[50] K.H. Lim, Z.X. Chen, K.M. Neyman, N. Rösch, J. Phys. Chem. B 110 (2006) 14890–14897.
[51] Z. Zhong, H. Ang, C. Choong, L. Chen, L. Huang, J. Lin, Phys. Chem. Chem. Phys. 11 (2009) 872–880.
[52] J.R. Roy, M.A. Laliberté, S. Lavoie, M. Castonguay, P.H. McBreen, Surf. Sci. 578 (2005) 43–56.
[53] M.C. Sanchez-Sanchez, R.M.N. Yerga, D.I. Kondarides, X.E. Verykios, J.L.G. Fierro, J. Phys. Chem. A 114 (2010) 3873–3882.
[54] M. Bowker, R. Holroyd, N. Perkins, J. Bhantoo, J. Counsell, A. Carley, C. Morgan, Surf. Sci. 601 (2007) 3651–3660.
[55] H. Guo, F. Zaera, J. Phys. Chem. B 108 (2004) 16220–16225.
[56] H. Guo, F. Zaera, J. Phys. Chem. B 108 (2004) 16226–16232.
[57] K.A. Dickens, P.C. Stair, Langmuir 14 (1998) 1444–1450.
[58] J. Llorca, N. Homs, P.R. de la Piscina, J. Catal. 227 (2004) 556–560.
[59] J.M. Guil, N. Homs, J. Llorca, P.R. de La Piscina, J. Phys. Chem. B 109 (2005) 10813–10819.